Spectral emission imaging to map photonic properties below the crystal surface of 3D photonic crystals

Christian Blum,[1] Allard P. Mosk,[2] Cees Otto,[1] Willem L. Vos,[2,3,4] and Vinod Subramaniam[1,5]

[1]*Biophysical Engineering Group, Faculty of Science and Technology and MESA+ Institute for Nanotechnology, University of Twente, P.O. Box 217, 7500 AE Enschede, The Netherlands*
[2]*Complex Photonic Systems (COPS), Faculty of Science and Technology and MESA+ Institute for Nanotechnology, University of Twente, P.O. Box 217, 7500 AE Enschede, The Netherlands*
[3]*Center for Nanophotonics, FOM Institute AMOLF, Kruislaan 407, 1098 SJ Amsterdam, The Netherlands*
[4]*w.l.vos@utwente.nl*
[5]*v.subramaniam@utwente.nl*

Received June 8, 2009; revised August 28, 2009; accepted September 11, 2009; posted September 22, 2009 (Doc. ID 112446); published October 16, 2009

We present the application of spectral emission imaging microscopy as a method to quantitatively map photonic properties from below the surface of strongly interacting photonic three-dimensional (3D) crystals. We excite emission from emitters deep inside a photonic crystal and record the local emission spectra with micrometer lateral resolution. The recorded directional emission spectra are modified by Bragg diffraction, which we use to determine the local stop-band attenuation, center frequency, and width. Assembling the values obtained into spatial maps yields detailed access to the distributions of the local photonic properties below the crystal surface. We demonstrate this approach by analyzing the emission from the fluorescent protein DsRed2 infiltrated inside self-organized 3D titanium dioxide inverse opals. © 2009 Optical Society of America

OCIS codes: 180.2520, 110.4234, 230.5298.

1. INTRODUCTION

Photonic metamaterials are currently the subject of intensive theoretical and experimental research as promising candidates to manipulate the coupling between light and matter and to control the properties of embedded light sources [1–5]. Examples of such metamaterials are disordered photonic glasses [6] or periodic photonic crystals with lattice spacings comparable to the wavelength of light. Photonic crystals control light propagation in particular crystallographic directions by means of Bragg interference, which results in wavelength ranges—called stop bands—for which light cannot propagate inside the crystal. The appearance of stop bands also modifies emission spectra of embedded light sources and gives rise to directional enhancements or attenuations [7–9]. Photonic crystals also control the local density of optical states, which determines the lifetime of excited light sources [2]. In the extreme case of a photonic bandgap, where a range of wavelengths is forbidden from propagation in all directions simultaneously, spontaneous emission is completely inhibited, which corresponds to infinite lifetimes [1].

Although tremendous progress has been made in the fabrication of photonic bandgap materials [10–13], all real photonic crystal structures inevitably suffer from intrinsic disorder, which leads to inhomogeneity of the photonic properties [14]. The visualization of the intrinsic disorder and its effect on the photonic properties has so far been limited to the surface or the first few layers of 3D photonic crystals: The structure of the surface of a photonic crystal can be imaged in great detail by scanning electron microscopy or atomic force microscopy [11,13,15,16]. Near field optical investigations have been used to study the photonic properties to characterize 3D photonic crystals; however, this technique probes evanescent waves that are limited to depths of a few hundred nanometers [17]. Reflection microscopy analyzes the local reflectivity of the photonic crystal [18–20] and yields information on the local photonic properties of the first few layers of the 3D photonic crystal, since light can penetrate into a photonic crystal only one Bragg length, which is typically a few micrometers. However, to fully exploit the unique properties of 3D photonic crystal structures, it is necessary to probe the photonic properties not only of the surface or the first few layers of the crystal, but also of the bulk crystal below. Knowledge of these properties will help to identify areas of high photonic quality on such metamaterials and to quantitatively characterize their local photonic parameters. The knowledge of the distribution of areas of differing photonic quality is an important element in attempts to improve the properties of photonic structures. Moreover, the optics of how light propagates from within a 3D photonic crystal as a Bloch mode to the outside world is still limited (for first attempts see, e.g., [21]). Thus, gathering such information will stimulate theory to this effect.

We show that analyzing the directed emission from emitters infiltrated into the 3D photonic crystal with micrometer spatial resolution can provide the desired insight into photonic crystal properties well below the surface at depths of several Bragg lengths. We use fluorescent proteins as emitters inside 3D photonic crys-

tals. Fluorescent proteins are extensively used in cell biology and a multitude of studies has addressed the emission properties of this important class of cellular markers [22–26]. We have recently shown that this class of biological fluorophores can also serve as efficient emitters inside photonic crystals [27]. In this study we have applied spectral imaging [28] to map photonic properties in 3D titanium dioxide inverse opals infiltrated with the fluorescent protein DsRed2. Based on the local emission spectra we quantitatively determine a number of parameters, such as the stop-band attenuation, stop-band center frequency, and relative width, which describe the local photonic properties. Finally, we assemble these parameters into maps to quantitatively visualize the photonic properties of the relevant domains and map their extent. The quantitative analysis of the local photonic crystal quality and the commensurate photonic parameters can be beneficial in the study of these crystals and their interaction with embedded light sources.

2. EXPERIMENTAL SECTION

Spectral emission imaging was achieved using a custom-built scanning stage confocal microscopy setup (for details see [29]). In short: for emission imaging the 488 nm line from a mixed gas Ar–Kr laser (Innova 70, Coherent, USA) served as the excitation source. For the reflectivity imaging a halogen lamp was used as the light source. The white light was relayed through two distant apertures to result in a well-collimated light beam. To minimize the influence from directional effects a low NA objective was used for excitation and detection. The excitation light was focused onto the sample by a 10× microscope objective (10×, 0.3 NA, Olympus, Japan). The sample was scanned by a piezoelectric scanning system composed of an electronic position controller (E-500, Physik Instrumente, Germany) and a scanning stage (P-740.20, 50×50 μm, Physik Instrumente, Germany). The fluorescence or reflected light was directed to the entrance pinhole (diameter of 10 μm) of a prism spectrometer. In emission imaging mode, reflected and scattered excitation light was suppressed by an appropriate holographic notch filter (Kaiser Optical Systems Inc., USA). The prism spectrometer was optimized for efficiency between 400 and 800 nm. Light was detected with a liquid nitrogen cooled charged-coupled device (CCD) camera (SPEC-10 System, Princeton Instruments, Trenton, New Jersey). The spectral resolution on the chip in the region where DsRed2 emits was ~1.0 nm. Spectral data were acquired using WINSPEC (Roper Scientific). The size of the pinhole, back projected to the sample, was ~5 μm as calculated from the magnification of the setup. This defines the area from which emission light is collected. However, the illumination light is focused to a smaller area of ~1 μm in diameter. We spectrally imaged our samples by raster scanning 50 ×50 μm areas of the photonic crystals recording 32×32 spectra per sampled area, resulting in one emission spectrum every 1.6 μm. Since the photonic effect observed builds up over some micrometers of photonic crystal (see discussion below), the axial resolution (~11 μm) is of secondary relevance.

Wide field emission imaging experiments were performed using a multimode microscopy setup (for details see [30]). A mercury lamp as the excitation source and a standard blue filter cube (U-MWB2, Olympus) were used. True color images were recorded with a color camera (AxioCam HRc, Zeiss). White balance was optimized for a halogen light temperature of 3200 K in accordance with the manufacturer's recommendation for fluorescence imaging. Contrast, brightness, and gamma correction were globally optimized for the whole images and no digital color changing filters were applied.

Titania inverse opals of lattice parameters of $a=440$ and 270 nm were produced according to [15]. In short: We fabricated in a first step opals from polystyrene colloidal particles, and then, after careful drying, deposited titania in the opal template by precipitation from alkoxide hydrolysis. Subsequently, the samples were heated to form anatase TiO_2 and to remove the polystyrene template, which resulted in an air-sphere crystal. The lattice parameter of the final crystals is controlled by the size of the polystyrene particles used. In Fig. 1(a) a scanning electron microscope image of the (111) face of a 3D titania inverse opal is presented. In the upper part of the image an area of highly ordered air spheres in titanium dioxide is visible, while the small black holes in each air sphere are windows connecting to the next layer of air spheres below. In the lower part of the depicted area the crystal is covered with unpatterned material.

The DsRed2 (Arg2Ala, Lys5Glu, Lys9Thr, Val105Ala, Ile161Thr, Ser197Ala) mutant of DsRed was produced by standard site-directed mutagenesis approaches as reported previously [31]. To infiltrate the fluorescent protein into the photonic crystals the aqueous protein solution was first desalted to prevent salt crystallization upon drying and then mixed with an equal volume of ethanol (Uvasol, Merck) to enhance the capability of the solution to penetrate the photonic crystal. The absorbance and emission spectra of DsRed2 in this water/ethanol mixture were indistinguishable from those of the protein in the buffer solution, indicating that the protein does not denature or aggregate in the water/ethanol mixture. Infiltration of DsRed2 into the inverse opals was achieved by soaking the crystals in the DsRed2 water/ethanol solution for 30 min. Finally, the crystals were rinsed with water (MilliQ, Millipore) for ~30 s to remove fluorescent proteins from the surface of the crystal and then dried overnight in a constant air flow.

The analyzed crystals had a size of about 1 mm ×1 mm and a thickness determined by the fabrication in a capillary of 200 μm. The photonic crystals were placed on a coverslip and imaged from above; all pictures and spectra were recorded normal to the $hkl=111$ planes of the crystal.

3. RESULTS AND DISCUSSION

A. Emission from Photonic Crystals

We used the visible fluorescent protein DsRed2 as an internal emitter inside titania inverse opals. In the study presented here we use the fact that the emission spectrum of visible fluorescent proteins is broad and that the fluorescing chromophore is encapsulated within a cylin-

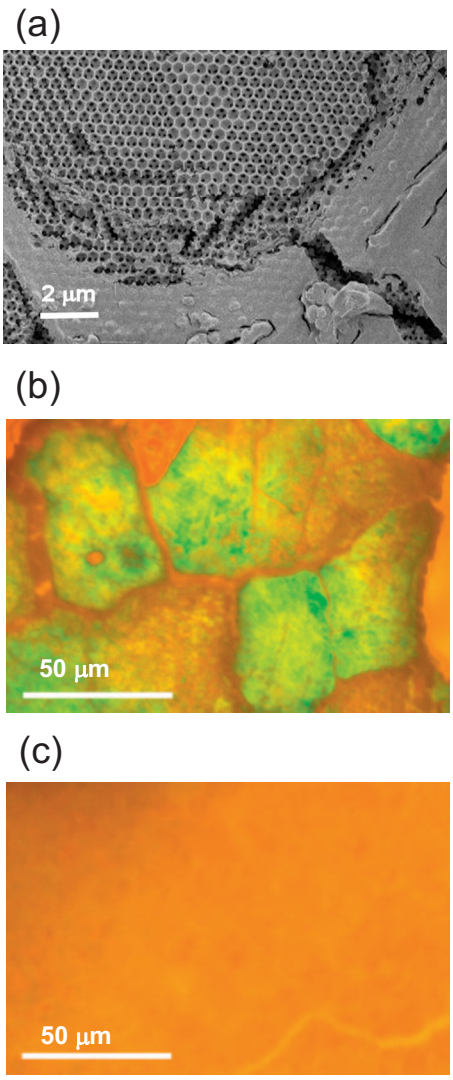

Fig. 1. (a) Scanning electron micrograph of a titania inverse opal showing the transition from an area of high (top) to an area of low (bottom) crystal quality. Although areas of high crystal quality clearly dominate, areas with different defects, cracks, and coverage with unpatterned material can be found. This inhomogeneity, and crystal characteristics in the depth of the photonic crystal invisible to scanning electron microscopy, result in differences in the optical properties in the different areas. (b) True color picture of the emission of DsRed2 in a titania inverse opal of lattice parameter $a=440$ nm. The attenuation and enhancement of the directional emission by Bragg diffraction on the crystal planes changes the apparent emission color of DsRed2 from orange-yellow to bright green. Large green areas are visible. Differences in the brightness and color hue indicate variations in the local photonic properties within these large photonic domains. Areas showing no clear sign of photonic modification of the emission color are visible in orange-yellow. (c) True color emission picture of DsRed2 in a titania inverse opal reference crystal of $a=270$ nm. The emission is orange-yellow and shows no significant lateral variations in color since the reference crystal has no photonic effect on the DsRed2 emission.

der formed by the protein backbone [32]. Only parts of the broad emission spectrum are influenced, even by strongly interacting photonic crystals showing a broad stop gap such as the titania inverse opals used here. In this study the broad emission spectrum is a decided advantage over quantum dots, which show a narrow emission spectrum that can be fully covered by a broad stop gap. When using quantum dots, the photonic attenuation by a photonic bandgap cannot be discriminated from a reduced emission intensity caused, e.g., by local variations in emitter concentration. The encapsulation of the chromophore in fluorescent proteins makes collisional quenching or quenching by electron transfer from the excited state to the conduction band of the titania unlikely. The latter effect is one that greatly hampers the use of conventional dyes as efficient emitters inside semiconductor photonic structures [33].

We have recently shown that titania inverse opals can be used to efficiently control the emission color of DsRed2 [27]. However, these crystals, like all real photonic crystals, show local variations in their photonic properties. Scanning electron micrographs show in detail that while the surface of these crystals is in most areas well ordered, surface defects occur, as do stress induced cracks and excess material deposited on the crystal surface (see Fig. 1(a); see also [15]). Imperfections inside the photonic crystals are not detectable by currently used techniques and it could well be that the crystal below the surface is not perfect. The combination of surface characteristics together with crystal features and defects hidden in the bulk of the crystal will lead to variations in the optical properties of the photonic crystal as illustrated in Fig. 1(b).

To quantitatively study the photonic effect of the inverse opals on the emission of DsRed2 a reference sample that offers the same chemical environment for the infiltrated emitter but with no photonic effect on the emission is needed. For that purpose we prepared and infiltrated crystals of a lattice parameter of $a=270$ nm with DsRed2. These crystals possess the same chemical properties as the photonic crystals used for the rest of this study, but have a stop band at shorter wavelengths where DsRed2 does not emit. Hence, emission from DsRed2 in these reference crystals is photonically unaltered and does not show significant variations in color [see Fig. 1(c)].

All sampled spectra from the reference crystal show the characteristic DsRed2 emission spectrum with emission maximum at $\sim 17000\ \mathrm{cm}^{-1}$. The emission maximum position is unchanged compared with that of the protein in aqueous solution, but the full width half maximum is increased to $2400\ \mathrm{cm}^{-1}$ compared with $1450\ \mathrm{cm}^{-1}$ in solution. We also observe a broadening of the emission spectrum of desalted DsRed2 upon drying on a coverslide. We therefore attribute the observed broadening to the possible loss of water embedded within the protein upon drying and the presence of titania in the close vicinity of the chromophore. The shape of the emission spectra did not show changes depending on the sampled position, but the intensity of the emission varied up to a factor of 15 between high and low emitting areas on a given crystal. We attribute this position dependence of the emission intensity to spatial heterogeneity of the doping. For example, one can easily envision higher infiltrated fluorophore concentrations along stress induced cracks in the crystal.

To estimate the influence of the intrinsic emission of the photonic crystal's backbone on the overall detected emission we applied identical experimental conditions to undoped reference crystals. We detect emission of low intensity, which agrees well with the reported anatase luminescence [34]. We find variations in the anatase emis-

sion intensity of about a factor of 5, yet the contribution of the titania emission to the detected overall emission of DsRed2 doped crystals is always minor [see Fig. 2(a)].

As a next step we infiltrated DsRed2 into titania inverse opals with lattice parameters of 440 nm. These crystals exhibit a photonic stop band visible as a frequency range with attenuated emission in the center of the emission band of DsRed2. We observed a strong position dependence of the shape of the detected emission spectra and of the intensity of the detected emission. To account for heterogeneous DsRed2 loading of the crystal we normalized the spectra to the red tail of the spectra (<14300 cm^{-1}) since in this spectral region the crystals show no photonic effect. In Fig. 2(a) we present a spectrum that is clearly different from the photonically undisturbed emission spectrum from the reference crystal. The most prominent alteration is the strong attenuation between 15 500 and 18 000 cm^{-1} which is in the exact frequency range where the photonic stop band, due to Bragg diffraction from the chosen photonic crystal, is expected to contribute to the directional emission of embedded emitters. The spectral position of the first order stop band can be calculated using Bragg's law using the lattice parameter of the crystal and the average refractive index based on the refractive indices of air and titania and the known titania filling fraction for the crystals used [15]. We calculate the stop-band center position for this crystal to be at 16 700 cm^{-1}.

B. Relative Intensity Spectra

To quantify the deviations of the emission spectrum caused by photonic effects of the crystal we divided the DsRed2 spectrum, normalized as detailed above, by the similarly normalized DsRed2 spectrum recorded from the reference titania inverse opal [see Fig. 2(a)]. We thus obtain a relative intensity spectrum that clearly highlights any attenuation or enhancement of emission relative to the photonically undisturbed spectrum. Attenuation and enhancement can quantitatively be explained by the escape function model [7]. Figure 2(b) depicts a typical example of an intensity ratio spectrum for the spectrum shown in Fig. 2(a).

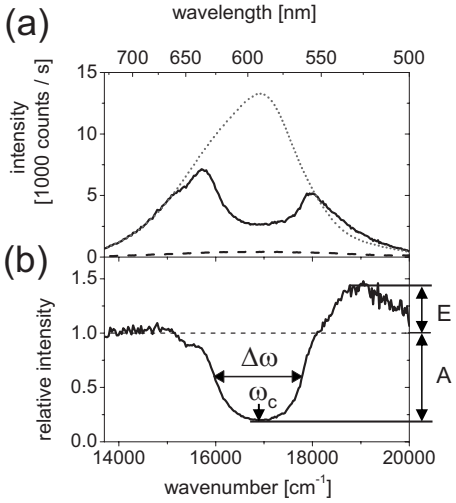

Fig. 2. (a) Emission from reference crystal of $a=270$ nm without (anatase emission only, dashed curve) and with infiltrated DsRed2 (gray dotted curve). The emission spectrum of DsRed2 inside a photonic crystal with nominal lattice parameter $a=440$ nm (black) shows a clear deviation from the spectrum not influenced by any photonic effect. The emission spectrum was normalized to the red tail of the reference spectrum (<14300 cm^{-1}) where the chosen crystals do not show any photonic effect. The intensity scale refers to the reference spectrum and confirms that the emission from the protein embedded in the crystal is intense. (b) Intensity ratio spectrum obtained by division of the modified by the reference spectrum. The stop band becomes apparent as a wavelength region of attenuation. On the blue side of the stop band, enhancement of the emission can be observed.

From the emission ratio spectra a number of parameters, such as the stop-band attenuation A, the enhancement E, the stop-band center frequency ω_c, and the stop-band width $\Delta\omega$ can be easily determined. The attenuation A is defined as the maximum deviation from 1, the stop-band width $\Delta\omega$ is defined as the width of the stop band at $0.5\,A$ and the center frequency ω_c is defined as the center between the two full width half maximum points of the attenuation [see Fig. 2(b)]. The extent of attenuation A and enhancement E are quantitative measures of the quality of the crystal since both parameters are directly linked to the amount of crystal imperfections and the mean free path [35]. The observed strong attenuation of the spectrum results from Bragg diffraction of the light of appropriate frequency in the direction of the detector. The enhancement E on the blue side of the stop band results from Bragg diffraction at higher angles. The deeper the stop band and the higher the enhancement on the blue side of the stop band the lower is the disorder in the sampled crystal position [7]. The stop-band center frequency ω_c is related to the size of the crystal's air spheres as well as to the average refractive index of the crystal. From the width $\Delta\omega$ and the center frequency ω_c of the stop band the relative width of the stop band can easily be calculated as the ratio between the width and the stop-band center frequency ($\Delta\omega/\omega_c$). This relative width is indicative of the photonic strength of the crystals [36].

C. Spatial Mapping of the Stop Band

Scanning spectral imaging shows evidence of a decided inhomogeneity of the local emission that agrees well with the expectations from wide field emission micrographs shown in Fig. 1(b). This approach, in which an area is raster scanned and an emission spectrum is recorded at each sampled point, generates a hyperspectral data cube containing local spectral information of the scanned area. From this data set, the local intensity ratio spectra are calculated as detailed above. Representative intensity ratio spectra are shown in Fig. 3(a). These spectra clearly show a stop band between 16 000 and 18 000 cm^{-1} but of variable attenuation and center frequency. The extent of the enhancement on the blue side of the stop band also exhibits significant variations. The attenuation A, enhancement E, stop-band center frequency ω_c, and width $\Delta\omega$ can be determined from the intensity ratio spectra for each sampled point and assembled into maps giving insights into the local photonic properties of the crystal. We present a typical attenuation map in Fig. 3(b).

The differences in attenuation are attributed to spatial variation of the amount of diffuse scattering by intrinsic disorder [35]. The attenuation map clearly shows the extent of one photonic domain of high crystal quality in the

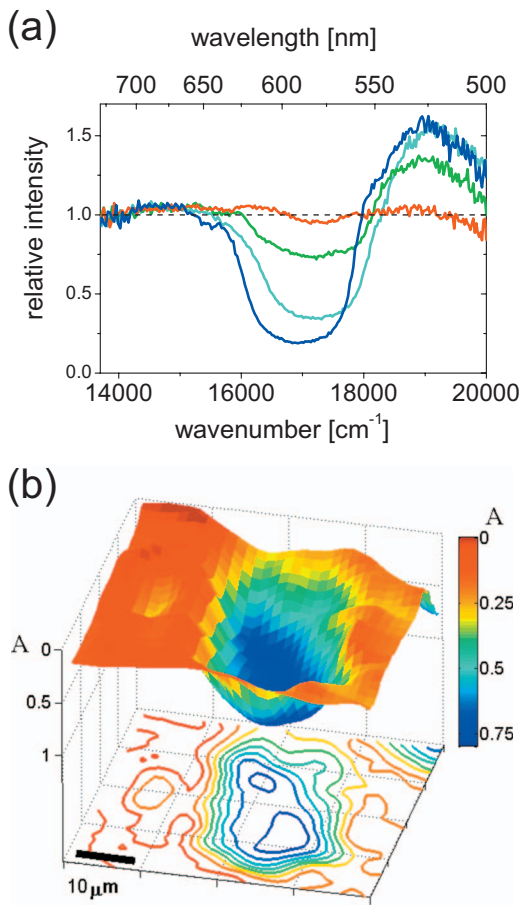

Fig. 3. (a) Intensity ratio spectra vary depending on the sampled position. Some of the ratio spectra show almost no deviation from the reference spectrum (red spectrum), while others show varying stop-band attenuation correlated with varying enhancement on the blue side of the stop band and stop-band center frequency and width. (b) An area of 50×50 μm was spectrally imaged recording 32×32 emission spectra. The intensity ratio spectrum and the attenuation A were determined at each position. The resulting attenuation values were assembled into a map using the same color coding as in (a). The map depicts strong attenuation in the center of the sampled region surrounded by a non-photonic or only weakly photonic region.

center of the sampled region [70%–85% attenuation; see blue intensity ratio spectrum in Fig. 3(a)]. The domain is surrounded by an area of little or no attenuation due to low crystal quality [see red intensity ratio spectrum; Fig. 3(a)]. Areas of intermediate crystal quality showing attenuation around 40% are also visible. Further, we observe a transition from no attenuation to very strong attenuation within approximately three pixels, which shows that the lateral resolution we achieve is not compromised by scattered light.

Identifying and mapping sample areas that show strong attenuation is the first step in the detailed characterization of the photonic properties of the sample. Based on the intensity ratio spectra [for examples see Fig. 3(a)], we deduced other relevant parameters and assembled the corresponding maps. Since the stop-band center frequency and the relative stop-band width can only be determined if a photonic effect in the form of a stop band is visible, the attenuation A is used as a threshold parameter. For all points fulfilling the criterion of attenuation larger than a threshold of $A=0.25$, we determined the stop-band center frequency and relative width. The attenuation, center frequency, and relative width maps for the data set shown in Fig. 3(b) are depicted in Fig. 4.

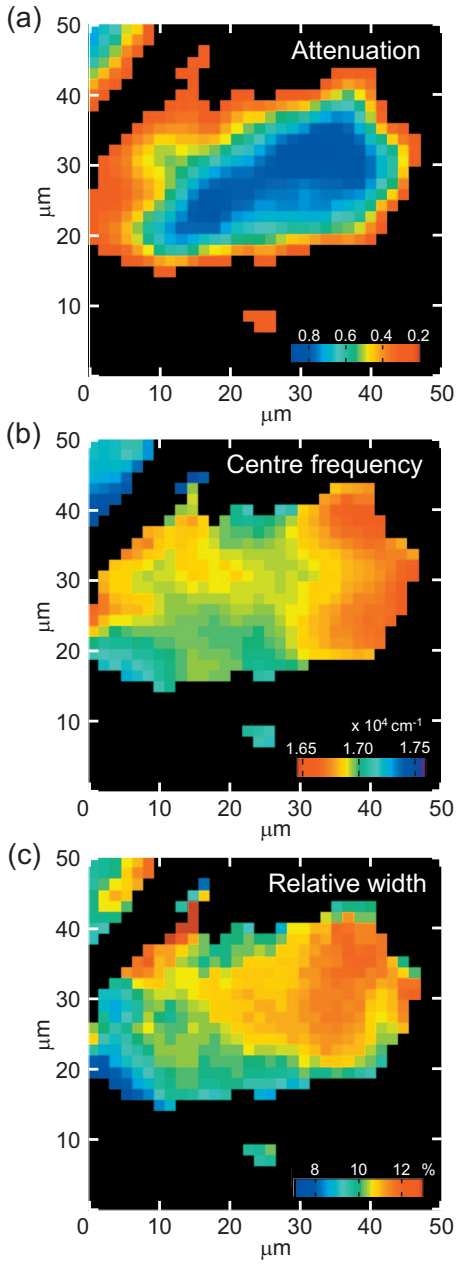

Fig. 4. (a) Map of the stop-band attenuation A shows the central photonic domain (around 28 μm, 26 μm) as well as the edge of a neighboring domain in the top left corner (~2 μm, 48 μm). The map shows the same area as shown in Fig. 3(b) using the same color scale. (b) The map of the stop-band center frequency ω_c shows a trend of increasing center frequency from right (~42 μm, 30 μm) to left (~5 μm, 18 μm) in the central domain. The neighboring domain clearly shows a decidedly higher center frequency. (c) The stop-band relative width map is calculated from the ratio of the stop-band width $\Delta\omega$ and center frequency ω_c ($\Delta\omega/\omega_c$). The relative width decreases from the right (~36 μm, 30 μm) to the left (~7 μm, 20 μm) in the central domain. A threshold of $A=0.25$ was used, since a noticeable stop band must be visible to determine its center frequency and width.

The different maps reveal the fine structure of the sampled domain. The attenuation map [Fig. 4(a)] clearly shows a roughly triangular region of very strong maximum attenuation between 70% and 85% together with a smaller plateau of attenuation between 40% and 50% ($\sim 12\ \mu m, 32\ \mu m$) for the central domain. The edge of a neighboring domain showing strong attenuation is visible in the top left corner of the sampled area ($\sim 2\ \mu m, 47\ \mu m$); a small area of minor attenuation ~25% is also visible ($\sim 4\ \mu m, 25\ \mu m$). The stop-band center frequency map [Fig. 4(b)] shows changes in the center frequency from $\sim 16\,650\ cm^{-1}$ at the right edge ($\sim 43\ \mu m, 30\ \mu m$) of the strongly attenuating center domain to $\sim 16850\ cm^{-1}$ at the left side of the domain ($\sim 5\ \mu m, 19\ \mu m$). Particularly interesting is the observation that the stop-band center frequency of the strongly attenuating neighboring domain visible at the top left corner ($\sim 2\ \mu m, 47\ \mu m$) of the image is moved to $\sim 17150\ cm^{-1}$. The relative width of the stop band agrees well with previous averaged results [10]. Nevertheless, assembling the detailed stop-band width map [Fig. 4(c)] of the photonic domain also shows a marked difference between the neighboring and the central domain. The relative width is increasing toward the left side of the central domain ($\sim 5\ \mu m, 18\ \mu m$).

Besides the amount of local defects (differences in A), variations in the titania filling fraction and of the air sphere radii, as have been observed before [15,37], are likely to play an important role in the observed variations in the stop-band width and center frequency. Finally, distinct steps in the stop-band center frequency from one domain to the next, as depicted in Fig. 4(b) between the main domain and the edge of the neighboring domain, are suggestive of an altered inclination of the lattice planes in this area with respect to the detector. Such a change in inclination is likely to be caused by a stress induced break and reorientation of parts of the crystal.

D. Subsurface Mapping

The objective of the method presented is to profile the photonic properties and hence the crystal quality from below the surface of strongly interacting photonic 3D crystals, a goal which is not accessible by current methods. The strong attenuation we observe is evidence that we sample emission from deeper inside the crystal than the Bragg attenuation length L_B. The Bragg attenuation length for titania inverse opals used in the present analysis was determined to be about seven crystal layers [19]. The observed attenuation in the stop band is determined by the ratio of the Bragg attenuation length and the transport mean free path l, which is the average distance light propagates before losing its initial direction due to scattering by defects and unavoidable variations in size and position of the building blocks of the photonic crystal [14]. Light propagates diffusely in the bulk of the crystal, since l is much smaller than the sample thickness. Light emanating, by emission or scattering, from $z < l$ propagates ballistically to the surface, while light emitted or scattered at $z < L_B$ is hardly Bragg attenuated. Hence, when a stop band is observed, emission originates from $L_B < z < l$. Using the estimation of the stop-band attenuation $A = 1 - (L_B/l)$ and the experimentally observed maximum stop-band attenuation of 85% observed for the crystal presented in Figs. 3 and 4, we find a mean free path of $l \sim 6.5^{*} L_B$. Since l represents the maximum depth that can be sampled using our method, the likely sampled depth is six and a half times larger than the depth sampled by Bragg reflection microscopy.

The added value of the capability to probe the photonic properties not only from the surface but also from deep within the crystal becomes directly visible when comparing reflectivity and emission images of the same region of a 3D photonic crystal. The attenuation map presented in Fig. 5(a) was obtained as detailed above. To determine the reflection enhancement by Bragg diffraction we spectrally imaged the same area using a white light source while spectrally recording the reflected light. Reflectivity intensity ratio spectra were obtained in a manner analogous to the method outlined for the emission spectra by normalization to a lamp reference spectrum and the blue wavelength tail of the reflected light. The reflection enhance-

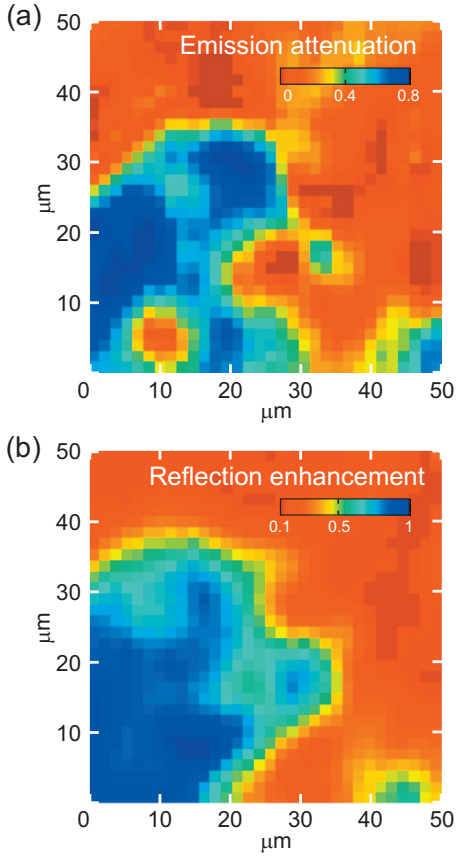

Fig. 5. (a) Stop-band attenuation map depicting the edge of a photonic domain. Attenuation maps report the photonic quality of the crystal area to a depth of the transport mean free path l. (b) Reflection enhancement map of the same area of the crystal. Analyzing the reflection of light from an external source only yields information about the first few layers of the crystal, since the light can only penetrate the Bragg length L_B into the crystal. The emission attenuation and the reflection enhancement map show clear differences. The most prominent difference is the area of low attenuation resembling low crystal quality in the depth of the crystal at the position ($\sim 10\ \mu m, 5\ \mu m$). At the same position in the reflection enhancement map very high reflection, resembling high surface quality of the crystal, can be observed. At this position bulk disorder is covered by a layer of very ordered crystal.

ment spectra clearly showed the enhanced reflectivity by Bragg diffraction, generally at the same wavelength and width as seen for the emission intensity ratio spectra from the same area. For each reflection enhancement spectrum the maximum was determined and the data were assembled into a reflectivity enhancement map shown in Fig. 5(b).

The differences between the emission attenuation map, displaying photonic properties up to a depth of the transport mean free path l below the crystal surface, and the reflection enhancement map, displaying photonic properties from the surface to a depth of only L_B, are obvious. The most prominent difference is the area of low attenuation at ($\sim$10 μm,5 μm), which is evidence of low crystal quality within the crystal, whereas the reflection image shows at the same position high reflection enhancement reporting a high crystal quality at the surface of the crystal. In this position bulk defects are covered by a layer of high crystal quality. This subsurface bulk disorder cannot be imaged with previously available surface imaging techniques. Similar differences between the emission attenuation and reflection enhancement map can be seen at the upper left edge of the photonic domain (e.g., $\sim$2 μm,30 μm) where the high quality surface expands further than the underlying bulk. The opposite can also be observed, namely, high attenuation due to high crystal quality below the surface coinciding with low reflectivity due to low crystal quality at the surface. An example of this can be seen at position ($\sim$25 μm,4 μm) where the area of high order extends further underneath a less ordered surface.

4. CONCLUSION

We have shown how spectral emission imaging can resolve the photonic properties from below the surface of 3D photonic samples. Spectral mapping of the directional emission from fluorophores infiltrated into the photonic crystal gives access to crystal properties down to several Bragg lengths below the surface of the crystal. Micrometer spatial resolution minimizes the influence of inhomogeneous broadening on the observed spectra that is usually seen when sampling larger areas at a time. The relative intensity spectra calculated from the local emission spectra clearly show the influence of Bragg diffraction on the local emission. Analyzing the relative intensity spectra yields detailed information on the local photonic properties and the data obtained can be assembled into maps clearly defining photonic domains of high photonic quality. The maps reflect the subsurface characteristics of the photonic crystal that are not accessible with current techniques that are limited to sampling the surface of the crystal. The maps can also be used to localize sample positions that show desired properties. We expect photonic domain mapping to be a valuable new tool to characterize photonic crystals to quantitatively determine local properties important for the accurate analysis of the interaction between embedded chromophores and the photonic crystal.

ACKNOWLEDGMENTS

We thank Léon Woldering and Charles Uju for fabricating inverse opals. This work is part of the research program of the "Stichting voor Fundamenteel Onderzoek der Materie" (FOM), which is supported by the "Nederlandse Organisatie voor Wetenschappelijk Onderzoek" (NWO). W. L. Vos also acknowledges NWO-Vici and STW/NanoNed.

REFERENCES

1. E. Yablonovitch, "Inhibited spontaneous emission in solid-state physics and electronics," Phys. Rev. Lett. **58**, 2059–2062 (1987).
2. P. Lodahl, A. F. van Driel, I. S. Nikolaev, A. Irman, K. Overgaag, D. L. Vanmaekelbergh, and W. L. Vos, "Controlling the dynamics of spontaneous emission from quantum dots by photonic crystals," Nature **430**, 654–657 (2004).
3. K. J. Vahala, "Optical microcavities," Nature **424**, 839–846 (2003).
4. W. L. Barnes, A. Dereux, and T. W. Ebbesen, "Surface plasmon subwavelength optics," Nature **424**, 824–830 (2003).
5. A. Badolato, K. Hennessy, M. Atature, J. Dreiser, E. Hu, P. M. Petroff, and A. Imamoglu, "Deterministic coupling of single quantum dots to single nanocavity modes," Science **308**, 1158–1161 (2005).
6. D. S. Wiersma, "The physics and applications of random lasers," Nat. Phys. **4**, 359–367 (2008).
7. I. S. Nikolaev, P. Lodahl, and W. L. Vos, "Quantitative analysis of directional spontaneous emission spectra from light sources in photonic crystals," Phys. Rev. A **71**, 053813 (2005).
8. A. Blanco, C. Lopez, R. Mayoral, H. Miguez, F. Meseguer, A. Mifsud, and J. Herrero, "CdS photoluminescence inhibition by a photonic structure," Appl. Phys. Lett. **73**, 1781–1783 (1998).
9. M. Barth, R. Schuster, A. Gruber, and F. Cichos, "Imaging single quantum dots in three-dimensional photonic crystals," Phys. Rev. Lett. **96**, 243902 (2006).
10. J. E. G. J. Wijnhoven and W. L. Vos, "Preparation of photonic crystals made of air spheres in titania," Science **281**, 802–804 (1998).
11. Y. A. Vlasov, X. Z. Bo, J. C. Sturm, and D. J. Norris, "On-chip natural assembly of silicon photonic bandgap crystals," Nature **414**, 289–293 (2001).
12. P. V. Braun, S. A. Rinne, and F. Garcia-Santamaria, "Introducing defects in 3D photonic crystals: state of the art," Adv. Mater. **18**, 2665–2678 (2006).
13. A. Blanco, E. Chomski, S. Grabtchak, M. Ibisate, S. John, S. W. Leonard, C. Lopez, F. Meseguer, H. Miguez, J. P. Mondia, G. A. Ozin, O. Toader, and H. M. van Driel, "Large-scale synthesis of a silicon photonic crystal with a complete three-dimensional bandgap near 1.5 micrometres," Nature **405**, 437–440 (2000).
14. A. F. Koenderink, A. Lagendijk, and W. L. Vos, "Optical extinction due to intrinsic structural variations of photonic crystals," Phys. Rev. B **72**, 153102 (2005).
15. J. E. G. J. Wijnhoven, L. Bechger, and W. L. Vos, "Fabrication and characterization of large macroporous photonic crystals in titania," Chem. Mater. **13**, 4486–4499 (2001).
16. F. Bresson, C. C. Chen, G. C. Chi, and Y. W. Chen, "Simplified sedimentation process for 3D photonic thick layers/bulk crystals with a stop-band in the visible range," Appl. Surf. Sci. **217**, 281–288 (2003).
17. E. Fluck, N. F. van Hulst, W. L. Vos, and L. Kuipers, "Near-field optical investigation of three-dimensional photonic crystals," Phys. Rev. E **68**, 015601 (2003).
18. Y. A. Vlasov, M. Deutsch, and D. J. Norris, "Single-domain spectroscopy of self-assembled photonic crystals," Appl. Phys. Lett. **76**, 1627–1629 (2000).
19. J. F. Galisteo Lòpez and W. L. Vos, "Angle-resolved reflectivity of single-domain photonic crystals: effects of disorder," Phys. Rev. E **66**, 036616 (2002).
20. G. M. Gajiev, V. G. Golubev, D. A. Kurdyukov, A. V. Medvedev, A. B. Pevtsov, A. V. Sel'kin, and V. V. Travnikov,

"Bragg reflection spectroscopy of opal-like photonic crystals," Phys. Rev. B **72**, 205115 (2005).
21. M. Doosje, B. J. Hoenders, and J. Knoester, "Scattering of light on the surfaces of photonic crystals," Opt. Commun. **206**, 253–258 (2002).
22. G. Jung, J. Wiehler, and A. Zumbusch, "The photophysics of green fluorescent protein: influence of the key amino acids at positions 65, 203, and 222," Biophys. J. **88**, 1932–1947 (2005).
23. Y. Cesa, C. Blum, J. M. van den Broek, A. P. Mosk, W. L. Vos, and V. Subramaniam, "Manipulation of the local density of photonic states to elucidate fluorescent protein emission rates," Phys. Chem. Chem. Phys. **11**, 2525–2531 (2009).
24. C. Blum and V. Subramaniam, "Single-molecule spectroscopy of fluorescent proteins," Anal. Bioanal. Chem. **393**, 527–541 (2009).
25. S. J. Remington, "Fluorescent proteins: maturation, photochemistry and photophysics," Curr. Opin. Struct. Biol. **16**, 714–721 (2006).
26. C. Blum, A. J. Meixner, and V. Subramaniam, "Spectral versatility of single reef coral fluorescent proteins detected by spectrally-resolved single molecule spectroscopy," ChemPhysChem **9**, 310–315 (2008).
27. C. Blum, A. P. Mosk, I. S. Nikolaev, V. Subramaniam, and W. L. Vos, "Color control of natural fluorescent proteins by photonic crystals," Small **4**, 492–496 (2008).
28. Q. S. Hanley, P. I. Murray, and T. S. Forde, "Microspectroscopic fluorescence analysis with prism-based imaging spectrometers: review and current studies," Cytometry A **69A**, 759–766 (2006).
29. G. M. J. Segers-Nolten, C. Wyman, N. Wijgers, W. Vermeulen, A. T. M. Lenferink, J. H. J. Hoeijmakers, J. Greve, and C. Otto, "Scanning confocal fluorescence microscopy for single molecule analysis of nucleotide excision repair complexes," Nucleic Acids Res. **30**, 4720–4727 (2002).
30. C. Blum, Y. Cesa, M. Escalante, and V. Subramaniam, "Multimode microscopy: spectral and lifetime imaging," J. R. Soc. Interface **6**, S35–S43 (2009).
31. C. Blum, A. J. Meixner, and V. Subramaniam, "Single oligomer spectra probe chromophore nanoenvironments of tetrameric fluorescent proteins," J. Am. Chem. Soc. **128**, 8664–8670 (2006).
32. F. Yang, L. Moss, and G. Phillips, "The molecular structure of green fluorescent protein," Nat. Biotechnol. **14**, 1246–1251 (1996).
33. P. V. Kamat, "Photochemistry on nonreactive and reactive (semiconductor) surfaces," Chem. Rev. **93**, 267–300 (1993).
34. R. Janes, M. Edge, J. Robinson, N. S. Allen, and F. Thompson, "Microwave photodielectric and photoconductivity studies of commercial titanium dioxide pigments: the influence of transition metal dopants," J. Mater. Sci. **33**, 3031–3036 (1998).
35. H. P. Schriemer, H. M. van Driel, A. F. Koenderink, and W. L. Vos, "Modified spontaneous emission spectra of laser dye in inverse opal photonic crystals," Phys. Rev. A **63**, 011801 (2000).
36. W. L. Vos, R. Sprik, A. Lagendijk, G. H. Wegdam, A. van Blaaderen, and A. Imhof, "Influence of optical band structures on the diffraction of photonic colloidal crystals," in *Photonic Band Gap Materials*, C. M. Soukoulis, ed. (Kluwer, 1996).
37. L. Bechger and W. L. Vos, "Homogeneity of oxide air-sphere crystals from millimeter to 100 nm length scales: a probe for macroporous photonic crystal formation," Chem. Mater. **16**, 2425–2432 (2004).